Λp interaction studied via femtoscopy in p + Nb reactions at $\sqrt{s_{NN}} = 3.18$ GeV

J. Adamczewski-Musch,[4] G. Agakishiev,[7] O. Arnold,[9,10,*] E. T. Atomssa,[15] C. Behnke,[8] J. C. Berger-Chen,[9,10] J. Biernat,[3] A. Blanco,[2] C. Blume,[8] M. Böhmer,[10] P. Bordalo,[2] S. Chernenko,[7] C. Deveaux,[11] A. Dybczak,[3] E. Epple,[9,10] L. Fabbietti,[9,10,*] O. Fateev,[7] P. Fonte,[2,†] C. Franco,[2] J. Friese,[10] I. Fröhlich,[8] T. Galatyuk,[5,‡] J. A. Garzón,[17] K. Gill,[8] M. Golubeva,[12] F. Guber,[12] M. Gumberidze,[5,‡] S. Harabasz,[5,3] T. Hennino,[15] S. Hlavac,[1] C. Höhne,[11] R. Holzmann,[4] A. Ierusalimov,[7] A. Ivashkin,[12] M. Jurkovic,[10] B. Kämpfer,[6,§] T. Karavicheva,[12] B. Kardan,[8] I. Koenig,[4] W. Koenig,[4] B. W. Kolb,[4] G. Korcyl,[3] G. Kornakov,[5] R. Kotte,[6] A. Krása,[16] E. Krebs,[8] H. Kuc,[3,15] A. Kugler,[16] T. Kunz,[10] A. Kurepin,[12] A. Kurilkin,[7] P. Kurilkin,[7] V. Ladygin,[7] R. Lalik,[9,10] K. Lapidus,[9,10] A. Lebedev,[13] L. Lopes,[2] M. Lorenz,[8] T. Mahmoud,[11] L. Maier,[10] S. Maurus,[9,10] A. Mangiarotti,[2] J. Markert,[8] V. Metag,[11] J. Michel,[8] C. Müntz,[8] R. Münzer,[9,10] L. Naumann,[6] M. Palka,[3] Y. Parpottas,[14,‖] V. Pechenov,[4] O. Pechenova,[8] V. Petousis,[14] J. Pietraszko,[4] W. Przygoda,[3] S. Ramos,[2] B. Ramstein,[15] L. Rehnisch,[8] A. Reshetin,[12] A. Rost,[5] A. Rustamov,[8] A. Sadovsky,[12] P. Salabura,[3] T. Scheib,[8] K. Schmidt-Sommerfeld,[10] H. Schuldes,[8] P. Sellheim,[8] J. Siebenson,[10] L. Silva,[2] Yu. G. Sobolev,[16] S. Spataro[¶] H. Ströbele,[8] J. Stroth,[8,4] P. Strzempek,[3] C. Sturm,[4] O. Svoboda,[16] A. Tarantola,[8] K. Teilab,[8] P. Tlusty,[16] M. Traxler,[4] H. Tsertos,[14] T. Vasiliev,[7] V. Wagner,[16] C. Wendisch,[4] J. Wirth,[9,10] J. Wüstenfeld,[6] Y. Zanevsky,[7] and P. Zumbruch[4]

(HADES Collaboration)

[1]*Institute of Physics, Slovak Academy of Sciences, 84228 Bratislava, Slovakia*

[2]*LIP - Laboratório de Instrumentação e Física Experimental de Partículas, 3004-516 Coimbra, Portugal*

[3]*Smoluchowski Institute of Physics, Jagiellonian University of Cracow, 30-059 Kraków, Poland*

[4]*GSI Helmholtzzentrum für Schwerionenforschung GmbH, 64291 Darmstadt, Germany*

[5]*Technische Universität Darmstadt, 64289 Darmstadt, Germany*

[6]*Institut für Strahlenphysik, Helmholtz-Zentrum Dresden-Rossendorf, 01314 Dresden, Germany*

[7]*Joint Institute for Nuclear Research, 141980 Dubna, Russia*

[8]*Institut für Kernphysik, Goethe-Universität, 60438 Frankfurt, Germany*

[9]*Excellence Cluster "Origin and Structure of the Universe", 85748 Garching, Germany*

[10]*Physik Department E12, Technische Universität München, 85748 Garching, Germany*

[11]*II. Physikalisches Institut, Justus Liebig Universität Giessen, 35392 Giessen, Germany*

[12]*Institute for Nuclear Research, Russian Academy of Sciences, 117312 Moscow, Russia*

[13]*Institute for Theoretical and Experimental Physics, 117218 Moscow, Russia*

[14]*Department of Physics, University of Cyprus, 1678 Nicosia, Cyprus*

[15]*Institut de Physique Nucléaire (UMR 8608), CNRS/IN2P3 - Université Paris Sud, F-91406 Orsay Cedex, France*

[16]*Nuclear Physics Institute, Czech Academy of Sciences, 25068 Rez, Czech Republic*

[17]*LabCAF, Facultad de Física, Universidad de Santiago de Compostela, 15706 Santiago de Compostela, Spain*

(Received 1 March 2016; published 4 August 2016)

We report on the first measurement of $p\Lambda$ and pp correlations via the femtoscopy method in p + Nb reactions at $\sqrt{s_{NN}} = 3.18$ GeV, studied with the High Acceptance Di-Electron Spectrometer (HADES). By comparing the experimental correlation function to model calculations, a source size for pp pairs of $r_{0,pp} = 2.02 \pm 0.01(\text{stat})^{+0.11}_{-0.12}(\text{sys})$ fm and a slightly smaller value for $p\Lambda$ pairs of $r_{0,\Lambda p} = 1.62 \pm 0.02(\text{stat})^{+0.19}_{-0.08}(\text{sys})$ fm are extracted. Using the geometrical extent of the particle-emitting region, determined experimentally with pp correlations as reference together with a source function from a transport model, it is possible to study different sets of scattering parameters. The $p\Lambda$ correlation is proven to be sensitive to predicted scattering length values from chiral effective field theory. We demonstrate that the femtoscopy technique can be used as a valid alternative to the analysis of scattering data to study the hyperon-nucleon interaction.

DOI: 10.1103/PhysRevC.94.025201

I. INTRODUCTION

The study of hyperon-nucleon and hyperon-nucleon-nucleon interactions has become more and more crucial in recent years due to its connection to the modeling of astrophysical objects such as neutron stars [1–4]. In the inner core of these objects the appearance of hyperons is a probable scenario since their creation is often energetically favored in comparison with a purely nucleonic matter composition. However, the appearance of these additional degrees of freedom leads to a softening of the matter equation of state (EOS) [5], making the latter incompatible with the recent

[*]Corresponding authors: oliver.arnold@mytum.de, laura.fabbietti@ph.tum.de

[†]Also at ISEC Coimbra, Coimbra, Portugal.

[‡]Also at ExtreMe Matter Institute EMMI, 64291 Darmstadt, Germany.

[§]Also at Technische Universität Dresden, 01062 Dresden, Germany.

[‖]Also at Frederick University, 1036 Nicosia, Cyprus.

[¶]Also at Dipartimento di Fisica and INFN, Università di Torino, 10125 Torino, Italy.

observation of neutron stars of two solar masses [6,7]. Many attempts were made to solve this "hyperon puzzle," e.g., by introducing three-body forces leading to an additional repulsion that counterbalances the large gravitational pressure and finally allows for larger star masses [8,9]. To constrain the parameter space of such models, a detailed knowledge of the hyperon-nucleon interaction (HNI) is mandatory.

Experimentally, the existence of hypernuclei [10] tells us that the HNI is attractive. An average value of $U(\rho = \rho_0, k = 0) \approx -30$ MeV is extracted from hypernuclear data [10] on the basis of a dispersion relation for hyperons in a baryonic medium at nuclear saturation density ($\rho_0 = 0.16$ fm^{-3}). But more detailed information in dense systems would be needed, in particular measurements as a function of the hyperon-nucleon relative momentum. Another experimental approach to studying the HNI is through scattering measurements where the hyperon-nucleon cross section can be obtained. Scattering lengths and effective ranges have thus been extracted from the available scattering data measured in the 1960s [11–13]. Together with the hypernuclear data, this has been so far the only possibility to constrain model predictions. Unfortunately, the statistics provided by scattering data is scarce, especially in the low momentum region, which is also the most sensitive for the determination of the scattering length. Theoretical calculations using a chiral effective field theory (χEFT) approach based on QCD motivated symmetries were performed at leading order (LO) and next-to-leading order (NLO), and values of the scattering length and effective range were computed [14]. Although these results differ, both confirm the attractiveness of the interaction for low hyperon momenta. In contrast to the LO results, the NLO solution claims the presence of a negative phase shift in the Λp spin singlet channel for Λ momenta larger than $P_\Lambda > 600$ MeV/c. This translates into a repulsive core of the interaction at small distances. Unfortunately, phase shifts can only be extracted from theoretical calculations but are not directly measurable in the ΛN case. This means that other techniques must be developed to verify the existence of a HNI repulsive core.

The possible presence of such a repulsive core could also be very important for the fate of neutron stars as it leads already to a certain repulsion in the EOS. With the inclusion of three-body interactions it is possible to make the hyperon matter even stiffer, eventually being able to overcome the two-solar-mass barrier set by measurements [15]. These three-body forces are poorly constrained and more work is needed to describe them properly.

This work presents an alternative to scattering experiments, using the femtoscopy technique to study the scattering lengths and effective ranges for hyperon-nucleon pairs produced in p + Nb collisions at 3.5 GeV kinetic energy. Furthermore, our results could provide additional constraints to theoretical model calculations.

Femtoscopy is based on the investigation of the correlation function of a particle pair at low relative momentum. The correlation signal present in this region is sensitive to the spatio-temporal extension of the particle-emitting source created, for example, in relativistic heavy-ion collisions [16,17]. Particle correlations are induced by quantum statistics in the case of identical particles as well as by final-state interactions (FSIs). Knowing the interaction of the particle pair precisely allows a detailed study of the geometrical extension of the emission region [18–23]. On the other hand, by reversing the paradigm, it is possible to study FSIs if the size of the particle source is already established. This is especially interesting in the case where the interaction strength is not well known [24–31]. We use the latter possibility for the investigation of the $p\Lambda$ interaction strength by comparing the experimentally obtained correlation function to a model containing results of scattering parameters calculated in the χEFT framework at LO and NLO. With the HADES setup the Λp correlation function was previously measured in Ar + KCl reactions [27].

In this work, we first reconstruct the size of the emission region which is created in p + Nb reactions by studying the correlation function of proton pairs. The interaction between protons is well understood, and additionally these baryon pairs obey similar kinematics as the $p\Lambda$ pairs. The ultrarelativistic quantum molecular dynamics (URQMD) [32,33] transport model is used to compare the $p\Lambda$ to the pp source sizes. This procedure allows one to fix the $p\Lambda$ source size and perform an investigation of the sensitivity of the method to different scattering length and effective range values.

The paper is organized in the following way: in Sec. II the experiment is briefly presented, and in Sec. III the correlation technique is discussed. Section IV shows the data selection and Sec. V the results obtained for the pp and Λp correlation function.

II. THE EXPERIMENT

The High-Acceptance Di-Electron Spectrometer (HADES) [34] is a fixed target experiment located in Darmstadt, Germany, at the GSI Helmholtzzentrum für Schwerionenforschung. Originally designed to measure low mass di-electrons originating from the decay of vector mesons, HADES is also well suited to measure charged hadrons with a good efficiency. The beams are provided by the synchrotron SIS18 with energies of 1–2 A GeV for heavy ions and up to 4.5 GeV for protons. Secondary pion beams with momenta up to 2 GeV/c are also available at this facility.

The detector system has an almost full azimuthal coverage, while the polar angles are covered from 18° to 85°. The achieved momentum resolution is $\Delta p/p \approx 3\%$. The multiwire drift chambers (MDCs)—two planes in front of and two behind the superconducting magnet (toroidal field)—and the Multiplicity and Electron Trigger Array (META) consisting of electromagnetic shower detectors (Pre-Shower) and time-of-flight scintillator walls (TOF and TOFINO) are the detector components which have been mainly employed in the analysis steps presented here. The hit points of the MDCs together with the bending of the tracks inside the magnetic field deliver the momentum information and the particle identification via the specific energy loss (dE/dx) for charged particles. The time-of-flight wall is also used to set the online trigger conditions.

In this analysis, data collected with a proton beam with a beam kinetic energy of $E_p = 3.5$ GeV incident on a twelvefold

segmented niobium target (^{93}Nb) with a beam intensity of $\sim 2 \times 10^6$ particles/s are studied. The nuclear interaction probability for this target was 2.8%. A first-level trigger (LVL1) was set requiring at least three hits in the time-of-flight wall (M3). In the whole run 3.2×10^9 events were collected.

III. CORRELATION FUNCTION

The observable used in femtoscopy to study the particle-emitting source and/or the particle interaction is the two-particle correlation function. This is defined as the ratio of the probability to find two particles with momenta $\mathbf{p}_1$ and $\mathbf{p}_2$ simultaneously and the product of the single particle probabilities:

$$C(\mathbf{p}_1,\mathbf{p}_2) \equiv \frac{P(\mathbf{p}_1,\mathbf{p}_2)}{P(\mathbf{p}_1)P(\mathbf{p}_2)}. \tag{1}$$

The probabilities are related to the inclusive invariant spectra $P(\mathbf{p}_1,\mathbf{p}_2) = E_1 E_2 \frac{d^6N}{d^3p_1 d^3p_2}$ and $P(\mathbf{p}_{1,2}) = E_{1,2}\frac{d^3N}{d^3p_{1,2}}$. Whenever the value of $C(\mathbf{p}_1,\mathbf{p}_2)$ deviates from unity, one measures a correlation between the particles. One of the goals is to use this correlation signal to conclude about the spatio-temporal extension of the particle-emitting source. Equation (1) can be reformulated as [17]

$$C(k) = \mathcal{N}\frac{A(k)}{B(k)}, \tag{2}$$

where k is the relative momentum of the pair defined as $k = |\mathbf{p}_1^* - \mathbf{p}_2^*|/2$, $\mathbf{p}_1^*$ and $\mathbf{p}_2^*$ being the momenta of the two particles in the pair rest frame (PRF). For identical particles k is linked to the one-dimensional Lorentz scalar $Q_{\rm inv} \equiv \sqrt{(\mathbf{p}_1 - \mathbf{p}_2)^2 - (E_1 - E_2)^2} = 2k$, also commonly used in femtoscopy analyses. $A(k)$ is the distribution of pairs from the same event and $B(k)$ is a reference sample of uncorrelated pairs. Usually, the latter is obtained by using an event mixing technique where the particles of interest are taken from different events. By construction, such a sample is free from two-particle correlations and represents the product of the single-particle probabilities. The factor $\mathcal{N}$ is determined by normalizing $C(k)$ to unity in the range of large relative momenta, in our case between $k \in [130,250]$ MeV/c for pp and $k \in [150,250]$ MeV/c for Λp pairs. These intervals were chosen in a region where the theoretical models deliver $C(k) = 1$ for the expected p + Nb source size. The chosen large relative momentum region should thus be free of any "femtoscopic" correlations.

The correlation function defined in Eq. (2) is integrated over all emission directions. For a more detailed study of the correlation signal including information about the emission direction, the longitudinally co-moving system (LCMS) can be used. The LCMS is defined as the rest frame along the beam axis where the z component of the total momentum of the pair vanishes, $\mathbf{P}_z = (\mathbf{p}_1 + \mathbf{p}_2)_z = 0$. The correlation function is calculated with the Cartesian "Bertsch-Pratt" or "out-side-long" conventions [17]. The "long" component ($k_{\rm long}$) is the longitudinal component pointing along the beam axis, whereas "out" ($k_{\rm out}$) and "side" ($k_{\rm side}$) are transverse to the beam direction by defining that the "out" component is aligned with the total transverse momentum $k_{\rm T} = |\mathbf{p}_{1\rm T} + \mathbf{p}_{2\rm T}|/2$ of the pair and "side" is perpendicular to "out" and "long." In the following, we will use the abbreviation "osl" to label the respective observables.

A. Femtoscopic and nonfemtoscopic correlations

To gain information about the size of the particle-emitting source, it is common to use certain approximations regarding the emission process and particle momenta involved in the reaction. Following [17], Eq. (1) can be rewritten as

$$C(\mathbf{P},\mathbf{k}) = \int d^3r^* S_{\mathbf{P}}(r^*)|\phi(r^*,\mathbf{k})|^2, \tag{3}$$

where the function $S_{\mathbf{P}}(r^*)$ represents the two-particle emission or source function containing the distribution of the relative distances of the pairs in the PRF (indicated by *). $\phi(r^*,\mathbf{k})$ is the pair relative wave function. The shape of the correlation function is determined by the wave function, which includes the particles interaction and their quantum statistics in the case of identical particles. For example, for pp correlations one has to take into account the Coulomb and strong interactions together with the antisymmetrization of the wave function [35]. The interplay of these three effects and the separation of the protons upon emission lead to a complex structure in the correlation function. The Coulomb interaction between the particles and the Pauli exclusion principle lead to a suppression of the correlation signal $C(k) < 1$ at very low $k \lesssim 10$ MeV/c, which increases by decreasing the source size. The attractive strong interaction in the s-wave channel leads to a positive correlation signal. As a result of these three effects, a characteristic bump structure appears around $k \approx 20$ MeV/c. The peak height of this bump increases for smaller proton source sizes.

In case of Λp pairs, the correlation signal is dominated by their attractive interaction only and is expected to be always positive. An analytical model describing the correlation between nonidentical baryon pairs was developed by Lednický and Lyuboshitz [36]. An application of this model to Λp correlations can be found in Ref. [24]. The model is based on an effective range expansion of the complex scattering amplitude $f^S(k) = (1/f_0^S + 1/2d_0^S k^2 - ik)^{-1}$, where S (=0,1) is the total spin of the particle pair, f_0^S is the scattering length, and d_0^S is the effective range. For a Gaussian emission profile of a source with radius r_0 the correlation function has the form [36]

$$C(k) = 1 + \sum_S \rho_S \left[\frac{1}{2}\left|\frac{f^S(k)}{r_0}\right|^2\left(1 - \frac{d_0^S}{2\sqrt{\pi}r_0}\right) + \frac{2\,\mathrm{Re}\, f^S(k)}{\sqrt{\pi}r_0}F_1(Q_{\rm inv}r_0) - \frac{\mathrm{Im}\, f^S(k)}{r_0}F_2(Q_{\rm inv}r_0)\right], \tag{4}$$

where $\mathrm{Im}\, f^S(k)[\mathrm{Re}\, f^S(k)]$ is the imaginary [real] part of the complex scattering amplitude, $F_1(z \equiv Q_{\rm inv}r_0) = \int_0^z dx \exp(x^z - z^2)/z$, and $F_2(z \equiv Q_{\rm inv}r_0) = [1 - \exp(-z^2)]/z$ are analytical functions resulting from averaging the square of the wave function over a Gaussian

source. The factor ρ_S contains the fraction of pairs emitted in a certain total spin state S. We assume unpolarized emission which translates into $\rho_0 = 1/4$ for the singlet state and $\rho_1 = 3/4$ for the triplet state.

Besides the femtoscopic correlations, there are additional correlations present, e.g., correlations due to energy and momentum conservation. These are usually washed out in large systems created in nucleus-nucleus collisions but show up for small systems, such as $p + p$, $e^+ + e^-$, or $p + A$ [37], where the particle multiplicities are lower. The inclusive particle spectra from the same event fulfill the constraints set by kinematics. But in the mixed-event sample this condition is not strictly matched. Hence, in the ratio of Eq. (2), an additional correlation is visible at large k, where the correlation function should otherwise be flat. These long range correlations (LRCs) could also have an influence at low momenta k, where an interplay between femtoscopy and momentum conservation effects takes place. We account for LRCs by introducing an additional correction correlation function which takes care of such momentum conservation effects, as explained in Sec. IV C.

IV. DATA ANALYSIS

A. Track selection

Particle tracks are selected requiring a good match between the track segment from the outer MDC and a META hit point. This selection is applied to get rid of fake and split tracks (one track is reconstructed as two tracks) which would introduce a fake positive correlation in the interesting region of low relative momenta. Another effect which distorts the correlation function stems from track merging. Particles in pairs of interest are emitted with small spatial separation and very homogeneously, meaning with very similar momenta and small opening angles. At a certain opening angle, the detector starts to merge two distinct tracks into one track because of the finite detector granularity. This effect introduces an artificial suppression of the yield in the same event distribution for low values of k. This is not the case for the mixed event sample, where only distinct tracks are combined by construction. To get rid of this track-merging effect, different correction methods were used, depending on the pair under investigation.

For pp pairs the following cuts were applied on the azimuthal and polar relative angles: $|\Delta\phi| > 0.12$ rad, $|\Delta\Theta| > 0.05$ rad. For Λp pairs a one-dimensional cut was used because of their limited statistics. The proton has a similar mass as the Λ, thus in the decay $\Lambda \to p\pi^-$ most of the decay momentum is transferred to the proton, keeping its flight direction similar to the Λ momentum vector, and as a consequence it also points back to the primary vertex. Hence, the primary and secondary protons are emitted with a small opening angle, leading possibly to track merging. To reject such pairs, a minimum opening angle of 5° (0.09 rad) between the primary and the secondary protons is applied. Both cuts were tested with the help of Monte Carlo simulations using URQMD as an event generator for pp and the Giessen-Boltzmann-Uehling-Uhlenbeck (GIBUU) [38] transport code for Λp pairs since GIBUU offers the possibility of scaling the production cross sections for channels including Λ hyperons. The events were filtered through the Geometry and Tracking (GEANT3) package

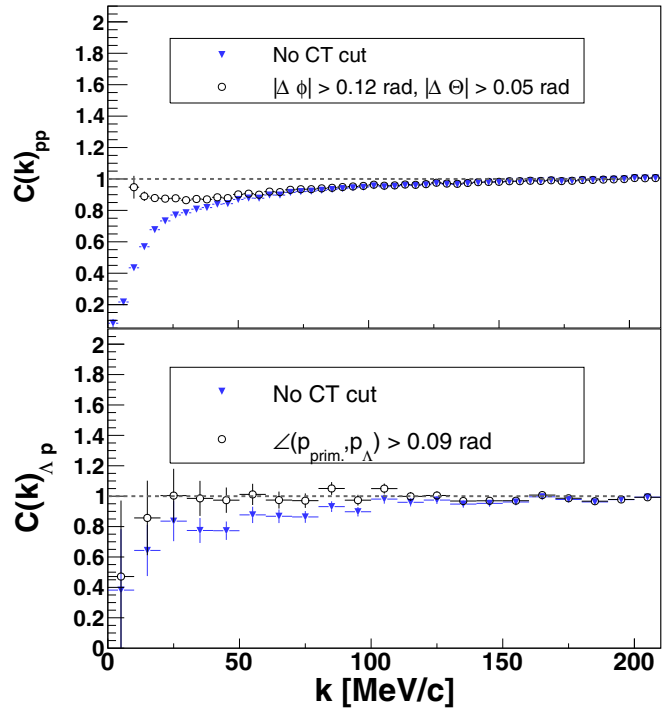

FIG. 1. Influence of the close track (CT) rejection on simulated 1D correlation functions for uncorrelated pp (top, URQMD) and Λp pairs (bottom, GIBUU). Open circles represent the correlation functions after the applied rejection cuts for close pairs while the (blue) triangles depict correlation signals without employing CT cuts.

to take the detector response into account. The effect of the close pair rejection on the correlation function for both types of pairs is illustrated in Fig. 1, where it is clearly visible that the merging is reduced after the cuts are applied. Only statistical errors are shown. Any remaining correlations are corrected for by introducing a new correlation function described in Sec. IV C. The chosen cut values and their stability were tested by varying them by 20% and the deviations on the final outcomes are included in a systematic error.

B. Protons and lambda hyperons

Proton identification is carried out by means of the specific energy loss information measured in the MDCs $[(dE/dx)_{\mathrm{MDC}}]$ as well as in TOF or TOFINO $[(dE/dx)_{\mathrm{TOF/TOFINO}}]$ as a function of the momentum and polarity of the particle. Figure 2 shows the distribution of the specific energy loss versus momentum times polarity of charged particles together with the two-dimensional graphical cuts used for the particle selection. Since TOF and TOFINO have different polar angle coverages and characteristic resolutions [34], they are treated separately and two additional graphical cuts are employed to select protons. For the Λp analysis only the energy loss information from the MDCs is used for particle identification to minimize the loss of statistics due to additional particle identification (PID) cuts. This results in a slightly worse proton purity (see Table II).

The Λ hyperon is identified via its charged $\Lambda \to p\pi^-$ decay products [39], where the branching ratio of this decay

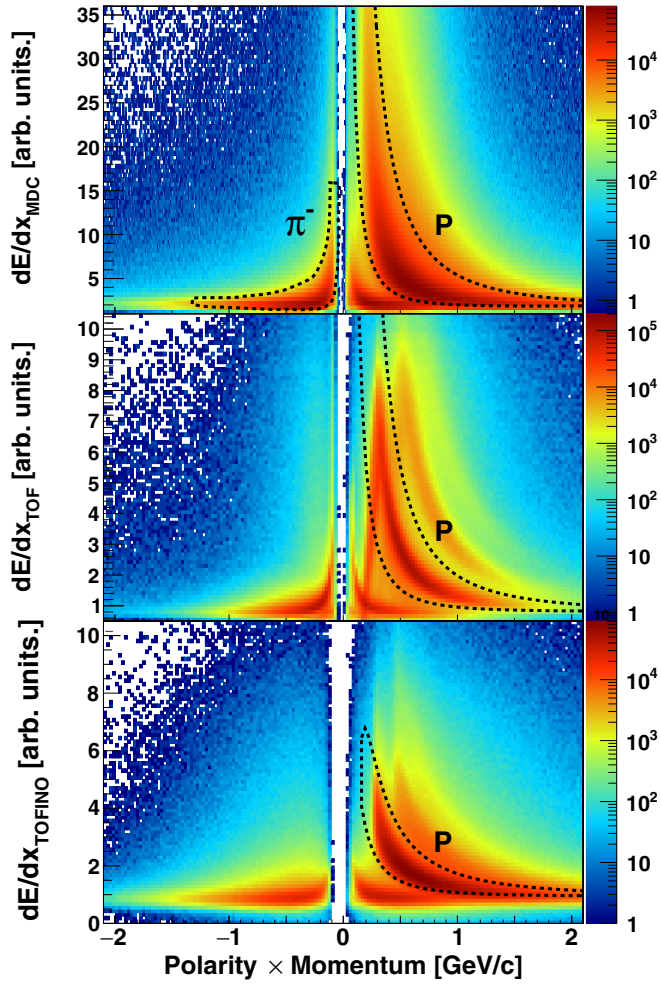

FIG. 2. Specific energy loss measured by the MDCs (upper row) as well as TOF (middle row) and TOFINO (bottom row) versus the product of the polarity and momentum of the particle. Particles are selected by two-dimensional graphical cuts depicted as dashed lines.

channel is 63.9% [40]. Because of the relatively long lifetime of the Λ ($c\tau = 7.89$ cm), it is possible to apply topological cuts to suppress the combinatorial background stemming mainly from direct $p\pi^-$ pairs. Four classes of topological cuts are used: (i) a cut on the distance of closest approach between the daughter tracks $\mathrm{DCA}_{p\pi^-}$, (ii) a cut on the distance of closest approach of the daughter tracks to the primary vertex DCA_p,DCA_{π^-}, (iii) a cut on the flight distance of the Λ hyperon evaluated as the distance between the secondary and primary vertex $d(|\mathrm{SV} - \mathrm{PV}|)$, and (iv) a cut on the "pointing angle" α between the spatial vector pointing from the primary to the secondary vertex and the Λ momentum vector. The cuts are optimized by requiring large Λ purities (>80%), minimizing at the same time the signal losses. The pointing angle and the distance of closest approach of the daughter tracks were fixed to $\alpha < 0.1$ rad and $\mathrm{DCA}_{p\pi^-} < 10$ mm for all the investigated cut combinations. The Λ candidates are constructed with the invariant mass of $p\pi^-$ pairs passing these topological cuts and selected in a 2σ interval around the nominal PDG mass [40]. Three different sets of topological cuts were tested to study the effect of different Λ signal purities in the data sample on the Λp correlation. A summary of the cut combinations and their corresponding purities can be found in Table I. An example of the Λ signal obtained for the most selective cut combination (combination 3) is shown in Fig. 3. To obtain the purity $P = S/(S+B)$, the background and signal are fitted simultaneously with a polynomial function for the background and two Gaussians for the signal peak. The number of reconstructed Λ's with this cut combination after the background subtraction amounts to $S(\Lambda) = (177.8 \pm 0.9) \times 10^3$.

TABLE I. Different topological cut combinations to select Λ candidates and the corresponding purities $S/(S+B)$. The values of the pointing angle $\alpha < 0.1$ and $\mathrm{DCA}_{p\pi^-} < 10$ mm were fixed.

Comb.	DCA_p (mm)	DCA_{π^-} (mm)	$d(\|\mathrm{SV} - \mathrm{PV}\|)$ (mm)	$S/(S+B)$
1	7	15	52	86.1%
2	7	25	57	89.6%
3	10	28	61	92.5%

For identified particle pairs the relative momenta are calculated in the PRF to obtain the same event distribution $A(k)$. For the reference sample $B(k)$ the event mixing technique is used. The events are selected according to the z-vertex position with a bin width of 6 mm for pp pairs and 10 mm for Λp pairs. This ensures that only events with similar geometrical acceptances are mixed. Additionally, for both types of pairs the events have been grouped in four multiplicity classes of bin width 2 for the multiplicity range $1 \leqslant M < 9$ and one class for $M \geqslant 9$ in order to mix only events with similar particle content and kinematics. Such a constrained mixing has been proved important in Ref. [41] in the case of cluster correlations.

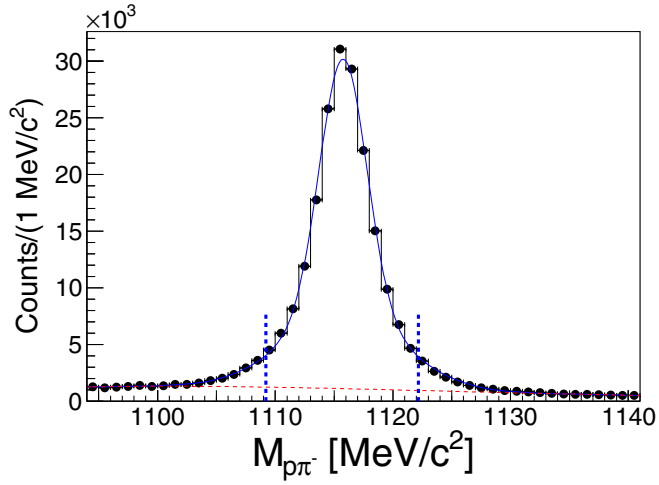

FIG. 3. Invariant mass distribution of $p\pi^-$ pairs after using topological cuts (combination 3 in Table I). Dots are for data, while the (blue) solid curve represents the fit of the signal and the (red) dashed line the background contribution. The two vertical (blue) dashed lines correspond to the 2σ region with $\sigma_\Lambda = 3.24 \pm 0.01$ MeV/c^2.

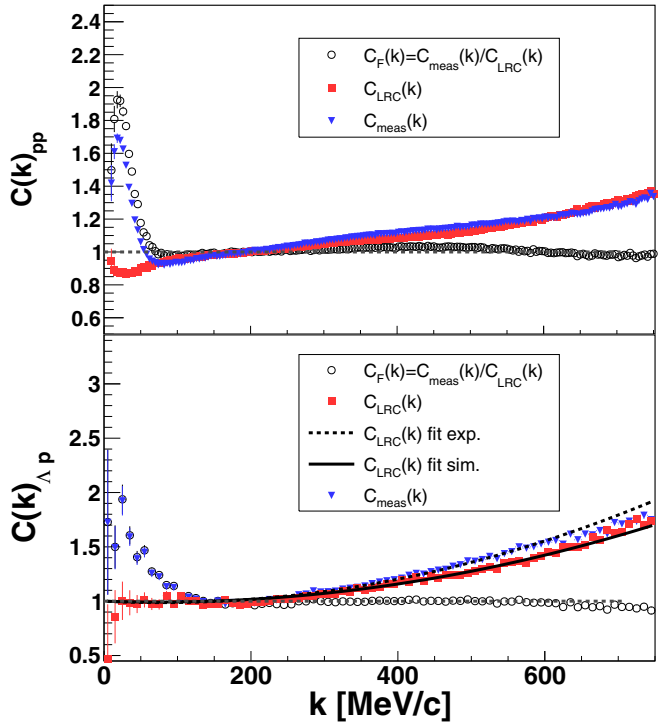

FIG. 4. Effects due to long-range correlations on the correlation function for pp pairs (top) and Λp pairs (bottom). The open circles depict the experimental correlation function corrected for long-range correlations. (Blue) triangles show the experimental function with long-range correlations inside and (red) squares the correlation function obtained from transport simulations. The solid and dashed lines in the lower panel show the fit with polynomial functions to the simulated and experimental LRCs, respectively. See text for details.

C. Corrections

As discussed in Sec, III, besides the femtoscopic correlations also correlations of nonfemtoscopic origin can show up in the correlation function. In the case of p + Nb collisions one deals with a small system which translates into a participant number of $A_{\rm part} \sim 2.5$ [39]. Since the average particle multiplicity per event is $\langle M \rangle \sim 4$, the total energy-momentum conservation for all registered particles is for event mixing more likely to be violated than in $A + A$ reactions. To disentangle correlation signals which are induced by energy and momentum conservation effects, semiclassical transport model simulations are used. These models are free from femtoscopic correlations but include correlations due to kinematic effects. The simulated events were filtered through the HADES acceptance and analyzed with the same cuts as for the experimental data. We used the same transport model predictions as were already used to determine the close track efficiency shown in Sec. IV A (URQMD for pp, GIBUU for Λp). The results of the calculations are depicted in Fig. 4. Both models reproduce the correlations reasonably well at large relative momenta. For this reason, a new variable is defined as the double ratio of the measured correlation function and the correlation function obtained from the simulated data:

$$C_F(k) = \frac{C_{\rm meas}(k)}{C_{\rm LRC}(k)}. \tag{5}$$

Because the simulated Λp correlation function suffers from larger statistical errors compared to the pp case at low k, the Λp baseline is fitted with a polynomial function in the range of [250,600] MeV/c. The employed polynomial is

$$C_{\rm LRC}(k) = 1 + ak + bk^2. \tag{6}$$

The obtained fit function is extrapolated to the region of low k and used to compute the ratio from Eq. (5). The result of the fit with the polynomial function (6) does not exhibit any significant differences when compared at low relative momenta to the experimental (dashed curve in Fig. 4, bottom panel) as well as to the simulated (solid curve in Fig. 4, bottom panel) correlation function baseline.

The HADES detector measures the single-particle momentum with a finite resolution which depends on the single-particle momentum itself and the emission polar angle [34], resulting in an uncertainty of the relative momentum k. A smearing of the pair momentum leads to a broadening of the correlation signal and thus to a systematic underestimation of the extracted source size. This is accounted for by a correction factor $K_{\rm mom}(k)$ [22]:

$$K_{\rm mom}(k) \equiv \frac{C_{\rm ideal}(k')}{C_{\rm smeared}(k)} = \frac{C_{\rm real}(k')}{C_F(k)}, \tag{7}$$

where $C_{\rm F}(k)$ is the measured correlation function of Eq. (5) corrected for LRC and $C_{\rm real}(k)$ is the correlation signal for a perfect momentum reconstruction. The ideal correlation function $C_{\rm ideal}(k)$ and the smeared correlation function $C_{\rm smeared}(k)$ are obtained from Monte Carlo mixed event samples for which the known ideal (input) momenta of the particles are subjected to the HADES momentum reconstruction procedure. To account for the smearing the following correlation functions are defined:

$$C_{\rm ideal}(k') = \frac{B(k', w(k'))}{B(k')}, \tag{8}$$

$$C_{\rm smeared}(k) = \frac{B(k, w(k'))}{B(k)}, \tag{9}$$

where $k' = |\mathbf{p}^*_{1,\rm ideal} - \mathbf{p}^*_{2,\rm ideal}|/2$ is calculated with the ideal input momenta and $k = |\mathbf{p}^*_{1,\rm smeared} - \mathbf{p}^*_{2,\rm smeared}|/2$ by using the reconstructed momenta. $B(k^{(\prime)})$ are the mixed event distributions and $B(k^{(\prime)}, {\rm w}(k'))$ are weighted by a correlation weight. The weight factor $w(k')$ is obtained by solving Eq. (3) assuming a Gaussian source profile and using the proper interaction for the pairs [42,43]. The source parameters are chosen such that the smeared correlation function (9) matches the experimental data. The relation (9) takes the effect of momentum smearing into account: The particles are correlated according to the ideal momentum k'; however, the detector reconstructs it with a finite resolution. The smeared correlation signal in Eq. (9) is obtained by weighting the smeared momentum distributions with the function w(k') evaluated for the ideal momentum. The influence of the corrections due to

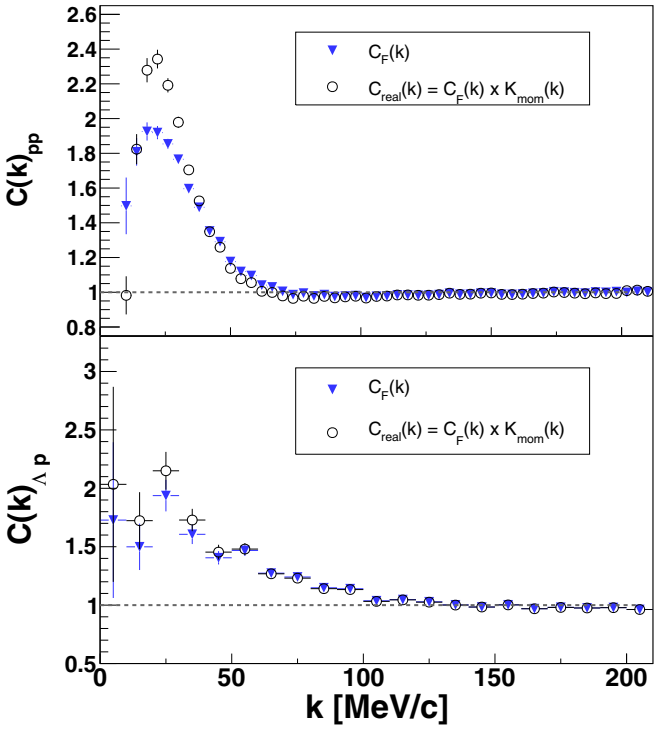

FIG. 5. Influence of the finite momentum resolution on the experimental correlation function for pp pairs (top) and Λp (bottom). Open circles display the unsmeared and (blue) triangles the smeared experimental correlation functions.

the momentum resolution on the correlation functions is shown in Fig. 5.

Particle misidentification reduces the correlation strength. This effect is corrected for by using the following relation [25,27]:

$$C_{\mathrm{pur,corr}}(k) = \frac{C_{\mathrm{pur,uncorr}}(k) - 1}{\lambda_{ab}} + 1, \qquad (10)$$

where $C_{\mathrm{pur,corr}}(k)$ and $C_{\mathrm{pur,uncorr}}(k)$ are the purity corrected and uncorrected correlation functions, respectively. Purity correction is the last correction step and for this reason $C_{\mathrm{pur,uncorr}}(k)$ is identical to $C_{\mathrm{real}}(k)$ of Eq. (7). The parameter λ_{ab} is the product of the PID purities of particles a and b.

Equation (10) is valid under the assumption that residual correlations between the particles can be neglected. Such correlations emerge when the original correlation between a parent pair is transferred partly to the daughter pair after the weak decay of one or both particles of the parent pair. We benefit from the rather low beam kinetic energy of 3.5 GeV, where the number of higher lying and long living baryon resonances is limited [44,45]. In the pp case it is ruled out by the available phase space in the final state that both protons originate from weak decays (e.g., $\Lambda\Lambda \rightarrow p_\Lambda p_\Lambda$). The fraction of protons stemming from a Λ decay compared to the total number of protons is about 0.003 estimated with URQMD simulations; thus, this feed-down can be neglected. This means that the proton correlation function is constructed with direct protons only.

TABLE II. Single-particle purities together with the two-particle purity parameter λ_{ab}.

Particle pair	Pur_a	Pur_b	λ_{ab}
pp	0.99	0.99	0.98
Λp (comb. 1)	0.86×0.82	0.97	0.68

The main feed-down to Λ is coming from Σ^0 decays. Σ^0 hyperons decay electromagnetically into the $\Lambda\gamma$ (100%) [40] final state and close to the production vertex because of the very short lifetime. This means that the measured Λ yield is a superposition of directly produced Λ plus the component coming from the feed-down of Σ^0. The ratio of directly produced Λ to all measured Λ was predicted by a statistical model analysis in p + Nb reactions to be $\Lambda/(\Lambda + \Sigma^0) = 0.82$ on the basis of the measured particle multiplicities [46]. To consider possible deviations from this predicted ratio we changed the value within a range of 10% and included the deviation of the Λp source size in the systematic errors. To model possible residual correlations having their origin from $p\Sigma^0$ pairs we have to take two aspects into account. First, the experimental information on the $p\Sigma^0$ interaction is rather scarce due to the difficulty of detecting the photon from the Σ^0 decay. Second, the $p\Sigma^0$ interaction needs for its description a larger parameter space than $p\Lambda$ because of two different total isospin configurations ($I = 1/2,3/2$), and the $I = 1/2$ configuration couples inelastically to the $p\Lambda$ channel. We studied residual correlations of $p\Sigma^0 \rightarrow p\Lambda_{\Sigma^0}$ with the help of [31,47] by calculating the $p\Sigma^0$ correlation function for a source size of 2 fm. After the decay into $p\Lambda_{\Sigma^0}$ a nearly flat uncorrelated behavior is extracted. This means that the already small $p\Sigma^0$ correlation is washed out after the decay. Experimental studies confirm the smaller interaction of $p\Sigma^0$ by measuring the energy dependence of the total cross section of $p\Lambda$ and $p\Sigma^0$ [48]. The $p\Sigma^0$ data is sufficiently described with a phase space parametrization whereas for the $p\Lambda$ case also final-state interactions had to be taken into account.

Finally, the purity parameters λ_{ab} were obtained with help of the URQMD event generator. The events where analyzed with the same graphical cut selections as applied to experimental data using the specific energy loss for the proton identification. The number of correctly identified protons is determined by this procedure and this purity calculated. The proton purity differs for the pp and Λp cases because we use only the MDC energy loss information for the proton identification in the Λp pair. The (primary) Λ purity is obtained from the invariant mass spectrum by calculating the background beneath the peak in a 2σ region around the pole mass times the fraction of directly produced Λ stated above. The obtained purities are listed in Table II.

V. RESULTS AND DISCUSSION

A. Source size extraction

After applying all corrections to the correlation functions, the first goal is to determine the size of the source where the particles are emitted from. The source size of pp and

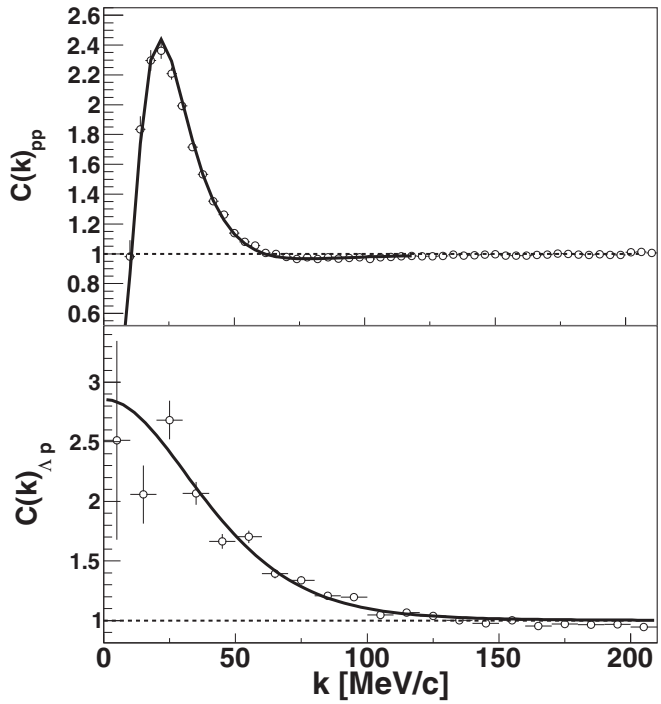

FIG. 6. Results of fitting Eq. (3) with a Gaussian source profile to the experimental pp correlation function (top) and the Lednický model Eq. (4) to the experimental Λp correlation function (bottom). Data are depicted by open circles.

Λp pairs can be extracted either by fitting the experimental correlation function or with the help of URQMD simulations. First, the fitting method is applied and the source size is extracted with help of solving Eq. (3) numerically for pp and the Lednický model of Eq. (4) for Λp. Both models assume a Gaussian source profile $d^3N/d^3r^* \sim \exp(-r^{*2}/4r_0^2)$, and for the pp interaction we use the strong interaction potential from [42]. The scattering length and effective ranges for the Λp interaction have been used from a NLO calculation for a cut-off of $\Lambda = 600$ MeV ($f_{0,\mathrm{NLO}}^{S=0} = 2.91$ fm, $d_{0,\mathrm{NLO}}^{S=0} = 2.78$ fm, $f_{0,\mathrm{NLO}}^{S=1} = 1.54$ fm, $d_{0,\mathrm{NLO}}^{S=1} = 2.72$ fm) [14]. Figure 6 shows the results from the fits that allow one to extract the radii. For pp pairs a source size of $r_{0,pp} = 2.02 \pm 0.01(\mathrm{stat})^{+0.11}_{-0.12}(\mathrm{sys})$ fm is obtained. The systematic errors are all quadratically added and estimated by variations of the close track rejection cuts, normalization of the correlation function, momentum resolution correction within 20%, and changing the interaction potential between the protons. For pp pairs it is also possible to investigate the source size as a function of the transverse momentum $k_T = |\mathbf{p}_{1,T} + \mathbf{p}_{2,T}|/2$ of the pair. Figure 7 shows the pp source radius as a function of k_T in an interval of [175,750] MeV/c. At higher transverse momenta we see a slow drop of the source size of about 13%. Such a decrease of the source radius is commonly measured in heavy-ion collisions where it arises from a collective expansion of the particle-emitting system inducing a correlation of coordinate and momentum space. But also in smaller and elementary systems a dependence on the transverse momentum is measured; see [49] and references therein. The rather moderate drop of

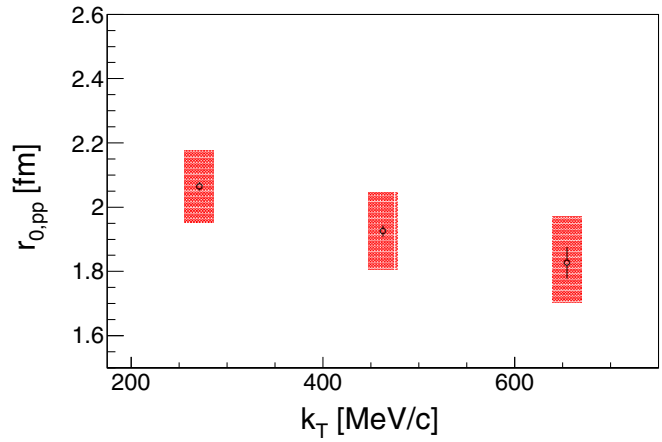

FIG. 7. Source size of pp pairs as a function of the total transverse momentum of the pair.

the pp source size could be an effect of the decreasing NN cross section in this momentum region. Rescattering of protons becomes less important going to larger k_T values which would be reflected in smaller source sizes. Such a behavior was also investigated in $e(4.46\ \mathrm{GeV}) + A$ reactions [50].

For the Λp source size we obtained a value of $r_{0,\Lambda p} = 1.62 \pm 0.02(\mathrm{stat})^{+0.19}_{-0.08}(\mathrm{sys})$ fm. The source size is smaller than the source extracted from pp correlations. Such an observation was also made in the Ar + KCl system [27]. In the p + Nb case, this is mainly due to the different scattering cross sections for pN and ΛN in the nucleus and to the different production processes. Indeed the scattering probability for ΛN is smaller than for NN (especially proton-neutron) scattering [40] which could lead to different emission times for protons. In a different study done by HADES using a statistical model approach to describe the particle multiplicities observed in the p + Nb system [46] it was also seen that the strangeness correlation radius $R_C = (1.5 \pm 0.8)$ fm is smaller than the correlation radius determined for nonstrange particles, $R = (2.0 \pm 0.6)$ fm.

The Gaussian radii extracted from the correlation functions may be compared to measurements from other experiments. For the $p\Lambda$ radius only data from heavy-ion collisions are available, which are difficult to compare with, since the emission regions in AA collisions are larger than in pA collisions. The invariant one-dimensional pp radii were measured by WA80 at SPS [51] [200A GeV, p + (Au,Ag,Cu,C)], NA44 at SPS [52] (450 GeV/c, p + Pb), and in the Fermilab H2-Ne bubble chamber experiment [53] (300 GeV/c, p + Ne) where radii of 2–6 fm were derived depending on the momentum interval of the emitted pair. In Fig. 8 we compare the HADES pp source radius obtained for p + Nb collisions to the measurements of WA80 and NA44 for medium size and large target nuclei. The derived source sizes sizes range from 1.4 to 2 fm and show a dependence on the target mass number in case of the WA80 data. Comparing similar systems sizes of p + Nb and p + Ag could hint at a energy dependence of the pp source radius on the beam energy. More data would be needed to clarify if such a trend exists.

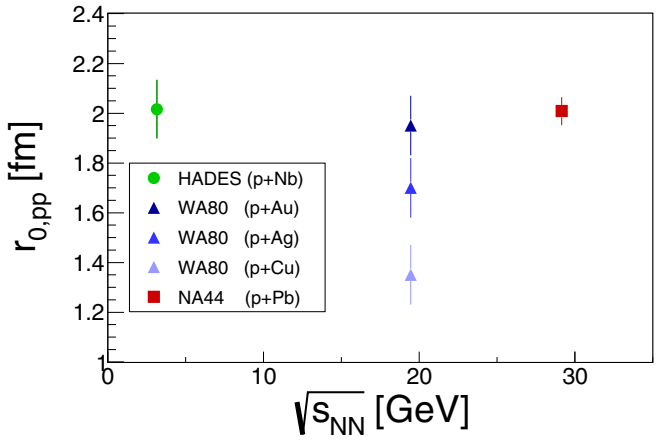

FIG. 8. Gaussian source radii evaluated from pp correlations in $p + A$ systems as a function of the nucleon-nucleon center-of-mass energy. The (green) full circle corresponds to the HADES measurement, blue triangles to data of WA80 [51], and the (red) square was derived by NA44 [52].

B. Λp final-state interaction

In order to extract the strength of the Λp FSI, the source size must be fixed. The URQMD simulation is used to determine the pp and Λp source for p + Nb reactions at 3.5 GeV. If the simulated pp source size is found to be consistent with the results from the fit shown in Fig. 6, the URQMD results for the Λp source can be used to fix r_0 in the Lednický model and test the final-state interaction. Polar acceptance cuts $\Theta \in [18^\circ, 85^\circ]$ are applied to the URQMD output to include the constraints by the HADES acceptance. Since URQMD is free from femtoscopy effects, an afterburner code, CRAB ($v3.0\beta$) [54], is used to include them. In CRAB the same pp potential was incorporated as the one used for the fitting of the experimental pp correlation function. A comparison of the one-dimensional (1D) and projections of the 3D correlation function calculated with URQMD+CRAB and the experimental data are displayed in Fig. 9. As can be seen in Fig. 9, URQMD+CRAB delivers a good description of the correlation signal for the 1D as well as for the 3D cases, hence the particle emission for protons is well implemented in the model, at least integrated over k_T.

For the determination of the Λp source size the URQMD model was slightly modified. URQMD uses the additive quark model (AQM) [55] for calculations of hyperon-nucleon (and the respective excited resonances) scattering cross sections. The derived AQM cross sections are independent of the energy involved in the scattering process. In particular, for the elastic cross section of Λp the value predicted by the AQM amounts to $\sigma \approx 37$ mb. However, measurements of the elastic Λp cross section show a strong rise for lower Λ momenta. Because we deal with low-energetic Λ hyperons at SIS18 beam energies, the cross section for elastic scattering was changed using the parametrization obtained from the χEFT-based LO and NLO calculations [14]. The LO as well as the NLO results take the rising of the total cross section into account.

To investigate the source size distribution the relative pairs distances in the LCMS are calculated and then boosted to the

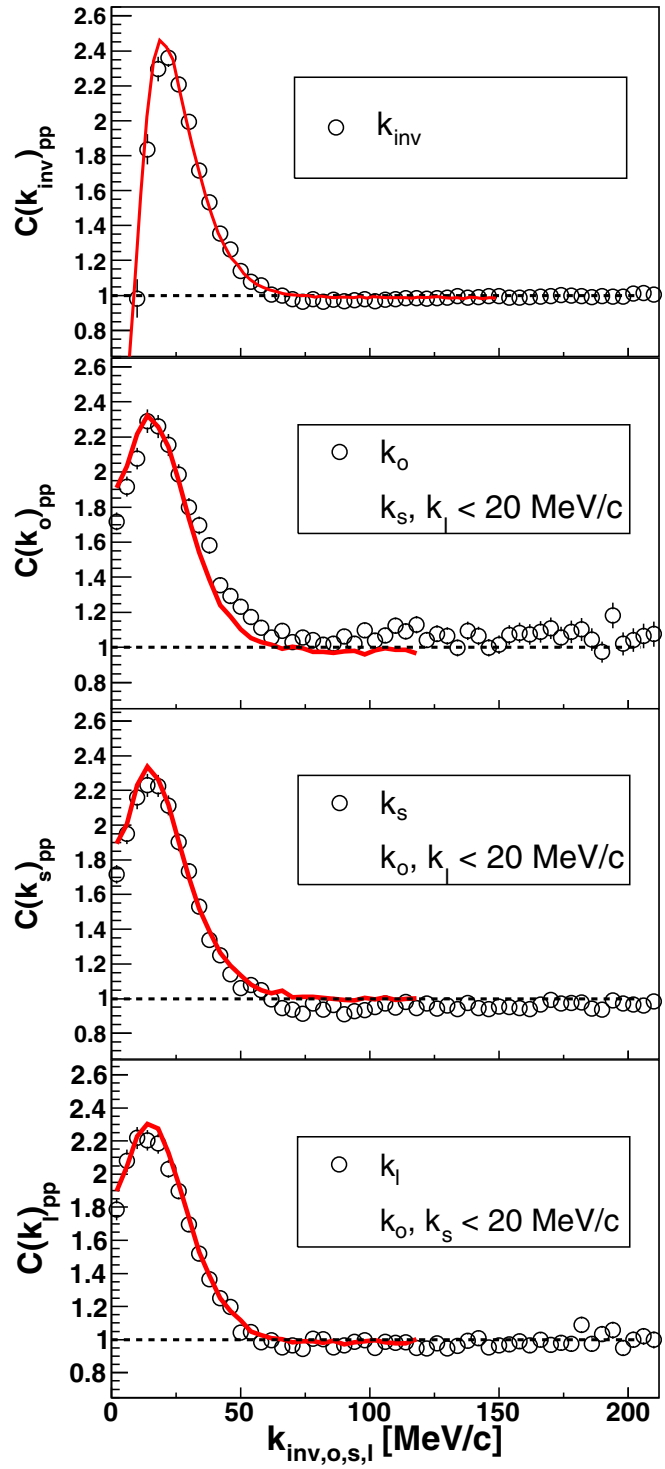

FIG. 9. Comparison of the experimental pp correlation function (open circles) with predictions from URQMD+CRAB (red solid line).

PRF [17]. The distribution of the relative coordinates in the PRF are depicted in Fig. 10 for Λp (blue triangles) and pp, respectively (open circles). Also in the URQMD calculations, the difference in the distributions for Λp and pp pairs points to different emission processes. To extract the radii, the distributions shown in Fig. 10 are fitted with a Gaussian

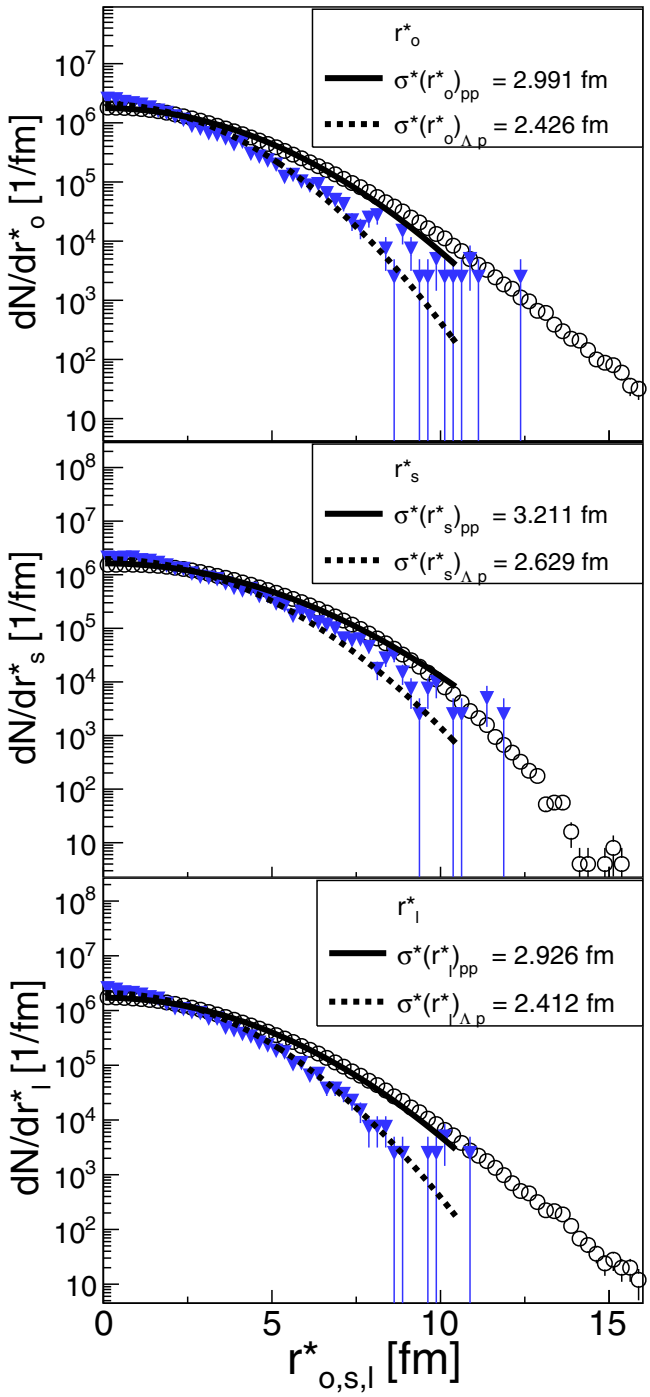

FIG. 10. Distribution of the relative distances obtained from URQMD simulations calculated in the PRF. Full triangles depict the outcome for Λp pairs (scaled to be shown with pp in one plot) and open circles are the result for pp pairs. The dotted and solid lines represent results of corresponding Gaussian fits according to Eq. (11).

function in the range $r^*_{o,s,l} \in [-10.5, 10.5]$ fm:

$$dN/dr^*_{o,s,l} \sim \exp\left\{-r^{*2}_{o,s,l}/\left(2\sigma^{*2}_{o,s,l}\right)\right\}. \tag{11}$$

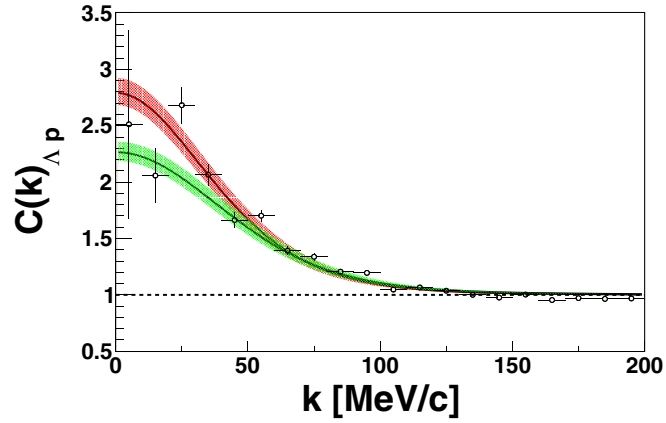

FIG. 11. Comparison of the experimental Λp correlation function (open circles with error bars) to the LO (green) and NLO (red) scattering parameter set included in Eq. (4). The error bands in the theory curves correspond to the errors of the Λp source size determination.

The widths $\sigma^*_{o,s,l}$ are related to the source size in the o,s,l directions as $\sigma^*_{o,s,l} = \sqrt{2} r^*_{o,s,l}$. The fit results are shown by the full lines in Fig. 10. A 1D emission width can be defined by averaging over all three emission directions [56]:

$$\sigma^*_{\text{inv}} = \sqrt{\frac{\sigma^{*2}_o + \sigma^{*2}_s + \sigma^{*2}_l}{3}}. \tag{12}$$

A ratio RF between the 1D radius obtained for pp and Λp pairs is defined ($\text{RF} = \sigma^*_{\text{inv},pp}/\sigma^*_{\text{inv},\Lambda p}$) and found to be equal to $\text{RF}_{\text{LO}} = 1.209$ and $\text{RF}_{\text{NLO}} = 1.222$ for the two different assumptions on the Λp cross section. The two results are rather similar which means that the source function does not strongly depend on the details of the Λp scattering. The source size measurement with pp pairs together with the above obtained source ratios leads to Λp source sizes of $r^{\Lambda p}_{0,\text{LO}} = 1.67^{+0.09}_{-0.10}$ fm, $r^{\Lambda p}_{0,\text{NLO}} = 1.66^{+0.09}_{-0.10}$ fm which are very similar to the one obtained by fitting the Λp correlation function directly. The errors of these source radii are dominated by the errors of the pp source size.

With the knowledge of the source radii we are in the position to test the LO and NLO predictions of scattering parameters. The values of the NLO scattering lengths and effective ranges were already mentioned in Sec. V A. For the LO parameters we take the results calculated at the same cutoff value of $\Lambda = 600$ MeV as for the NLO case ($f^{S=0}_{0,\text{LO}} = 1.91$ fm, $d^{S=0}_{0,\text{LO}} = 1.40$ fm, $f^{S=1}_{0,\text{LO}} = 1.23$ fm, $d^{S=1}_{0,\text{LO}} = 2.13$ fm) [14]. A comparison of the correlation functions using the LO (green band) and NLO (red band) scattering parameters is shown in Fig. 11.

It is obvious that the two theoretical correlation functions differ at low relative momenta where their behaviours are mainly governed by the scattering length, and the effective range plays a minor role. The colored bands associated to the theoretical calculations are obtained by varying the Λp source radius within the errors. Unfortunately, the statistics analyzed here is not sufficient to draw a definite conclusion. However, the method appears sensitive to different scattering

length parameters and represents an alternative to scattering experiments used to study the hyperon-nucleon interaction in detail. In particular, there are no scattering data available at all in the region of very low relative hyperon-nucleon momentum ($k < 50$ MeV/c).

VI. SUMMARY

To summarize, we have presented the first measurement of the $p\Lambda$ correlation function in pA reactions. The pp correlation signal was used as a benchmark to test the possibility of fixing the source size on the basis of URQMD calculations. This way, the Λp source was estimated. The finalstate interaction strength between $p\Lambda$ was investigated by comparing the experimental $p\Lambda$ correlation function to model calculations using scattering parameters from χEFT computations. The statistics was not enough to clearly distinguish between model predictions (an increase by a factor of 10 would be sufficient). It was, however, shown that the femtoscopy method is able to provide data which can be investigated with a theoretical framework with the necessary sensitivity to study carefully final-state interactions if the size of the particle-emitting region is known beforehand. The application of femtoscopy to study interactions between particles is possible in many colliding systems at very different energies, which can help to improve the understanding of hyperon-nucleon interactions. With the planned upgrade of the HADES setup with an electromagnetic calorimeter, the measurement of the $p\Sigma^0$ correlation function is accessible and it is a planned analysis in the HADES strangeness program.

ACKNOWLEDGMENTS

The authors are grateful to M. Bleicher for stimulating discussions. The HADES Collaboration gratefully acknowledges support by the grants LIP Coimbra, Coimbra (Portugal); PTDC/FIS/113339/2009 SIP JUC Cracow, Cracow (Poland); NCN grant 2013/10/M/ST2/00042, Helmholtz-Zentrum Dresden-Rossendorf (HZDR), Dresden (Germany); BMBF 06DR9059D, TU München, Garching (Germany); MLL München, DFG EClust 153, VH-NG-330; BMBF 05P15WOFCA, DFG FA898/2-1, GSI TMLRG1316F; GACR 13-067595, NPI AS CR, Rez (Czech Republic); MSMT LC07050 GAASCR IAA100480803 USC - S. de Compostela, Santiago de Compostela (Spain); CPAN: CSD2007-00042 Goethe-University, Frankfurt (Germany); HA216/EMMI HIC for FAIR (LOEWE); and BMBF: 06FY9100I GSI FE EU Contract No. HP3-283286.

[1] S. Petschauer, J. Haidenbauer, N. Kaiser, U.-G. Meißner, and W. Weise, Eur. Phys. J. A **52**, 15 (2016).
[2] H. J. Schulze, A. Polls, A. Ramos, and I. Vidana, Phys. Rev. C **73**, 058801 (2006).
[3] S. Weissenborn, D. Chatterjee, and J. Schaffner-Bielich, Nucl. Phys. A **881**, 62 (2012).
[4] S. Weissenborn, D. Chatterjee, and J. Schaffner-Bielich, Phys. Rev. C **85**, 065802 (2012); **90**, 019904(E) (2014).
[5] H. Đjapo, B.-J. Schaefer, and J. Wambach, Phys. Rev. C **81**, 035803 (2010).
[6] P. Demorest, T. Pennucci, S. Ransom, M. Roberts, and J. Hessels, Nature (London) **467**, 1081 (2010).
[7] J. Antoniadis *et al.*, Science **340**, 1233232 (2013).
[8] Y. Yamamoto, T. Furumoto, N. Yasutake, and T. A. Rijken, Phys. Rev. C **88**, 022801 (2013).
[9] Y. Yamamoto, T. Furumoto, N. Yasutake, and T. A. Rijken, Phys. Rev. C **90**, 045805 (2014).
[10] O. Hashimoto and H. Tamura, Prog. Part. Nucl. Phys. **57**, 564 (2006).
[11] B. Sechi-Zorn, B. Kehoe, J. Twitty, and R. A. Burnstein, Phys. Rev. **175**, 1735 (1968).
[12] F. Eisele, H. Filthuth, W. Foehlisch, V. Hepp, and G. Zech, Phys. Lett. B **37**, 204 (1971).
[13] G. Alexander, U. Karshon, A. Shapira, G. Yekutieli, R. Engelmann, H. Filthuth, and W. Lughofer, Phys. Rev. **173**, 1452 (1968).
[14] J. Haidenbauer, S. Petschauer, N. Kaiser, U. G. Meissner, A. Nogga, and W. Weise, Nucl. Phys. A **915**, 24 (2013).
[15] D. Lonardoni, A. Lovato, S. Gandolfi, and F. Pederiva, Phys. Rev. Lett. **114**, 092301 (2015).
[16] S. Pratt, Phys. Rev. D **33**, 1314 (1986).
[17] M. A. Lisa, S. Pratt, R. Soltz, and U. Wiedemann, Annu. Rev. Nucl. Part. Sci. **55**, 357 (2005).
[18] V. Henzl *et al.*, Phys. Rev. C **85**, 014606 (2012).
[19] G. Agakishiev *et al.* (HADES Collaboration), Eur. Phys. J. A **47**, 63 (2011).
[20] R. Kotte *et al.* (FOPI Collaboration), Eur. J. Phys. A **23**, 271 (2005).
[21] M. M. Aggarwal *et al.* (WA98 Collaboration), arXiv:0709.2477.
[22] J. Adams *et al.* (STAR Collaboration), Phys. Rev. C **71**, 044906 (2005).
[23] K. Aamodt *et al.* (ALICE Collaboration), Phys. Lett. B **696**, 328 (2011).
[24] J. Adams *et al.* (STAR Collaboration), Phys. Rev. C **74**, 064906 (2006).
[25] T. Anticic *et al.* (NA49 Collaboration), Phys. Rev. C **83**, 054906 (2011).
[26] P. Chung *et al.*, Phys. Rev. Lett. **91**, 162301 (2003).
[27] G. Agakishiev *et al.* (HADES Collaboration), Phys. Rev. C **82**, 021901 (2010).
[28] L. Adamczyk *et al.* (STAR Collaboration), Phys. Rev. Lett. **114**, 022301 (2015).
[29] L. Adamczyk *et al.* (STAR Collaboration), Nature (London) **527**, 345 (2015).
[30] V. M. Shapoval, B. Erazmus, R. Lednicky, and Yu. M. Sinyukov, Phys. Rev. C **92**, 034910 (2015).
[31] A. Kisiel, H. Zbroszczyk, and M. Szymanski, Phys. Rev. C **89**, 054916 (2014).
[32] S. Bass, M. Belkacem, M. Bleicher, M. Brandstetter, L. Bravina *et al.*, Prog. Part. Nucl. Phys. **41**, 255 (1998).
[33] M. Bleicher *et al.*, J. Phys. G **25**, 1859 (1999).
[34] G. Agakishiev *et al.* (HADES Collaboration), Eur. Phys. J. A **41**, 243 (2009).
[35] S. E. Koonin, Phys. Lett. B **70**, 43 (1977).
[36] R. Lednicky and V. L. Lyuboshits, Yad. Fiz. **35**, 1316 (1981) [Sov. J. Nucl. Phys. **35**, 770 (1982)].

[37] B. Abelev *et al.* (ALICE Collaboration), Phys. Rev. D **87**, 052016 (2013).
[38] O. Buss, T. Gaitanos, K. Gallmeister, H. van Hees, M. Kaskulov, O. Lalakulich, A. B. Larionov, T. Leitner, J. Weil, and U. Mosel, Phys. Rep. **512**, 1 (2012).
[39] G. Agakishiev *et al.* (HADES Collaboration), Eur. Phys. J. A **50**, 81 (2014).
[40] K. Olive *et al.* (Particle Data Group), Chin. Phys. C **38**, 090001 (2014).
[41] B. Kampfer *et al.*, Phys. Rev. C **48**, R955 (1993).
[42] B. D. Day, Phys. Rev. C **24**, 1203 (1981).
[43] A. R. Bodmer and Q. N. Usmani, Phys. Rev. C **31**, 1400 (1985).
[44] G. Agakishiev *et al.* (HADES Collaboration), Phys. Lett. B **742**, 242 (2015).
[45] G. Agakishiev *et al.* (HADES Collaboration), Phys. Rev. C **87**, 025201 (2013).
[46] G. Agakishiev *et al.* (HADES Collaboration), Eur. Phys. J. A **52**, 178 (2016).
[47] A. Stavinskiy, K. Mikhailov, B. Erazmus, and R. Lednicky, arXiv:0704.3290.
[48] M. Abdel-Bary *et al.* (COSY-TOF Collaboration), Eur. Phys. J. A **46**, 27 (2010); [**46**, 435(E) (2010)].
[49] G. A. Nigmatkulov *et al.*, Phys. Lett. B **753**, 458 (2016).
[50] A. V. Stavinsky *et al.* (CLAS Collaboration), Phys. Rev. Lett. **93**, 192301 (2004).
[51] T. Awes *et al.*, Z. Phys. C **65**, 207 (1995).
[52] H. Boggild *et al.* (NA44 Collaboration), Phys. Lett. B **458**, 181 (1999).
[53] S. A. Azimov *et al.*, Phys. Rev. D **29**, 1304 (1984).
[54] F. Wang and S. Pratt, Phys. Rev. Lett. **83**, 3138 (1999).
[55] K. A. Goulianos, Phys. Rep. **101**, 169 (1983).
[56] A. Kisiel, Phys. Rev. C **81**, 064906 (2010).